Microinstabilities in hydrogen- and helium-dominated multi-ion-species plasmas in LHD

Microinstabilities in hydrogen- and helium-dominated multi-ion-species plasmas in LHD

Masanori Nunami[1,2], Motoki Nakata[1,2], Hideo Sugama[1,2], Kenji Tanaka[1,3] and Shinichiro Toda[1]

[1]National Institute for Fusion Science, National Institutes of Natural Sciences, Toki, Gifu 509-5292, Japan

[2]The Graduate University for Advanced Studies, Toki, Gifu 509-5292, Japan

[3]Kyushu University, Department of Advanced Energy Engineering, Kasuga, Fukuoka 816-8580, Japan

E-mail: nunami.masanori@nifs.ac.jp

Abstract. The ion scale microinstabilities in the Large Helical Device (LHD) are investigated by the gyrokinetic simulations for the multi-ion-species plasmas including hydrogen, helium, and impurity ions. The observations in the LHD experiments show that the ion temperature increases with the decreases of the ratio of hydrogen density to helium density. It is found from the linear gyrokinetic simulations with the multi-ion-species and real-mass kinetic electrons in the LHD discharges that the growth rates of the ion scale microinstabilities are reduced for the helium-dominated multi-species plasma compared with the hydrogen-dominated one. In addition to the differences of the conditions including the temperature, the density profiles, and the temperature ratio between both plasmas, due to the dependence on the mass number and the electric charge of the mixed ion species, the mixing length estimates obtained from the linear simulations predicts smaller ion thermal diffusivity for the helium-dominated plasma than the hydrogen-dominated one in the hydrogen gyro-Bohm unit, which is consistent with the experimental results.

Keywords: Microinstabilities, Gyrokinetic simulation, Large Helical Device

1. Introduction

Quantitative predictions of anomalous transport fluxes of particles and heat in magnetically confined plasmas are critical issues to design the fusion reactors. The gyrokinetic approaches[1] are powerful to analyze the transport phenomena driven by the drift-wave plasma turbulences, and a lot of validation studies[2, 3, 4, 5, 6, 7, 8] of the gyrokinetic simulations against the experimental results have been performed. In addition to the validation studies, the modeling for the turbulent transport have been done[9] in order to predict the transport fluxes with reduced calculation costs.

Nowadays, understanding of the transport phenomena in the mixed plasma consists of multi-ion species is strongly demanded for burning plasma studies in the ITER or future fusion reactors, and near future planned deuterium experiments in the Large Helical Device (LHD)[10]. In the deuterium LHD experiments[11], effects of different hydrogen isotopes on the transport and the confinement performances should be clarified. For the hydrogen isotope plasma transport, we have to treat the complicated physics including the effects of the mass, charge, and some resulting phenomena, i.e., the electric field and so on. In the linear trapped electron mode (TEM) instability analyses[12], the TEM is stabilized in the deuterium plasma through the ion-mass dependence in the ratio of the electron-ion collision frequency to the ion transit frequency, i.e., $\nu_{\rm ei}/\omega_{\rm ti} \propto (m_{\rm i}/m_{\rm e})^{1/2}$.

On the other hand, in recent LHD experiments, the ion internal transport barriers (ITB) in the mixed species plasma which includes hydrogen and helium[13] was observed. In the experiments, it was found that the ion temperature depends on the density ratio of hydrogen ions to helium ions, and the ion temperature is higher in the low hydrogen density ratio than the high hydrogen ratio case, under the almost same heating power. These experiments should be considered as a significant reference for the transport characteristics of different ion species. In this paper, we investigate the transport phenomena of the mixed plasma consists of hydrogen, helium, and a few impurity ions by the microinstabilities analyses using the gyrokinetic turbulence code which can treat the multi-species plasmas including real-mass kinetic electrons. In particular, the ion-scale microinstabilities such as the ion temperature gradient (ITG) mode are evaluated for different LHD plasmas, i.e., hydrogen-dominated multi-species plasmas and helium-dominated one.

This paper is organized as follows. In Sec. 2, we briefly describe the results observed in the LHD experiments for hydrogen- and helium-dominated multi-ion-species plasmas. In Sec. 3, the simulation model used in the paper and basic equations employed in the calculation are explained. In Sec. 4, we show the results of the gyrokinetic analyses for the ion scale microinstabilities in both cases, the hydrogen- or the helium-dominated plasmas in the LHD. Finally, we summarize the work in Sec. 5.

2. Ion temperature in hydrogen- and helium-dominated plasmas in LHD experiment

In the LHD experiments[13], the ITB was observed with helium gas puffing and the neutral beam injection (NBI) heating. The ratio of hydrogen density to the helium density, $n_{\rm H}/(n_{\rm H}+n_{\rm He})$, was scanned from 0.34 to 0.78 on shot by shot basis by changing the gas puff from helium to hydrogen under the almost same heating power. The power depositions per ion $P_{\rm i}/n_{\rm i}$ are almost same in these experiments[14]. Figure 1 shows the radial profiles of the ion and electron temperatures and their radial gradients R_0/L_T in steady phases of two discharges at $t = 4.74$ s in the LHD discharges of #128670 and #128717, where $L_T^{-1} \equiv -d\ln T/dr$ and the major radius R_0. Here, we assume that each ion has same temperature. In Fig. 2, the densities and their radial gradients

R_0/L_n of each species are shown. Here, there are three ion species (hydrogen, helium, and carbon) in the discharges, and $L_n^{-1} \equiv -d\ln n/dr$. In the case of #128670, the hydrogen/helium ratio is $n_{\rm H}/(n_{\rm H}+n_{\rm He}) = 0.34$ (helium-dominated case) and the case of #128717 corresponds to $n_{\rm H}/(n_{\rm H}+n_{\rm He}) = 0.78$ (hydrogen-dominated case). The ion temperature in the helium-dominated case is higher than the hydrogen-dominated case with similar electron temperature. While the temperature ratio between electron and ions $T_{\rm e}/T_{\rm i}$ in the helium-dominated case is lower than that in the hydrogen-dominated case, the normalized $T_{\rm i}$- and $T_{\rm e}$-gradient scale lengths are almost identical with each other in the both cases. On the other hand, higher $T_{\rm i}$ in the helium-dominated plasma is achieved at the edge region $\rho > 0.8$. Since the $T_{\rm i}$-gradient scale lengths are almost identical with each other, the high-$T_{\rm i}$ at the edge region may cause the core high-$T_{\rm i}$ in the helium-dominated case. More detail studies about these points with the experimental observations including characteristics of measured ion scale turbulence will be reported[14]. The increasing temperature ratio between the electron and the ions, $T_{\rm e}/T_{\rm i}$ can enhances the growth rates of the microinstabilities[12]. Therefore, in the hydrogen-dominated case, the ITG mode growth rates in the physical unit can be more enhanced than the helium-dominated case. As shown in Fig. 3, it is also found that the ion temperatures at the magnetic axis $r/a \equiv \rho = 0$ strongly depend on the density ratio of hydrogen to helium, while the electron temperature does not depend on the ratio. Here, a is the minor radius. In the experiments, we can estimate the total ion heat diffusivities by the power balance analysis using TASK3D-a code[15], as shown in Fig. 4. In the helium-dominated case, the obtained diffusivity normalized by the gyro-Bohm factor of the hydrogen defined as $F_{\rm GB}^{\rm (H)} \equiv \alpha(\rho_{\rm t}/R_0)cT_{\rm i}/Z_{\rm H}eB$ is smaller than the hydrogen-dominated case[14]. Here, α is the arbitrary constant which is fixed in both cases, and $\rho_{\rm t}$ is the thermal gyro-radius of hydrogen which equals that of helium ions, $\rho_{\rm tH} = \rho_{\rm tHe}$, for each experimental shot where the two species are assumed to have the same temperature.

3. Gyrokinetic simulation model

In this paper, we employed the gyrokinetic local flux-tube turbulence code GKV [16, 17, 18], which has been extended to treat multi-species plasmas including precise collision operator [19, 20], for the analyses of the microinstabilities in the LHD plasmas introduced in the previous section. In the GKV code, the time evolution of the wavenumber-space representation of electromagnetic gyrokinetic equation is solved for the perturbed gyrocenter distribution function of species s, $\delta f_{sk_\perp} = -e_s J_{0s}\delta\phi_{k_\perp}F_{{\rm M}s}/T_s + h_{sk_\perp}$, where $h_{sk_\perp}$ is the non-adiabatic part of the perturbed distribution function. The gyrokinetic equation for the non-adiabatic part can be represented by

$$\left(\frac{\partial}{\partial t} + v_\parallel \boldsymbol{b}\cdot\nabla + i\omega_{{\rm D}s} - \frac{\mu \boldsymbol{b}\cdot\nabla B}{m_s}\frac{\partial}{\partial v_\parallel}\right) h_{sk_\perp} - \frac{c}{B}\sum_{\Delta} \boldsymbol{b}\cdot(\boldsymbol{k}'_\perp \times \boldsymbol{k}''_\perp)\delta\psi_{k'_\perp} h_{sk''_\perp}$$
$$= \frac{e_s F_{{\rm M}s}}{T_s}\left(\frac{\partial}{\partial t} + i\omega_{*Ts}\right)\delta\psi_{k_\perp} + C_s(h_{sk_\perp}). \qquad (1)$$

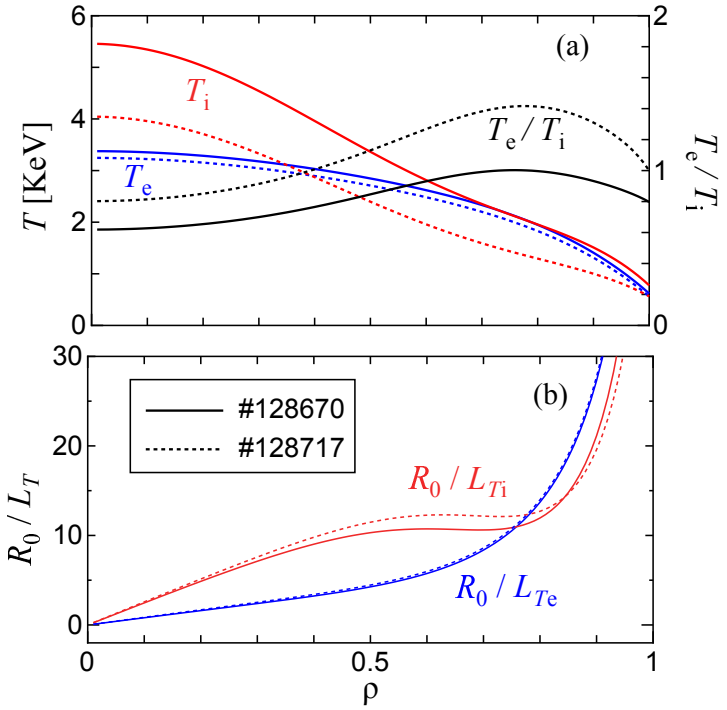

Figure 1. (a) Radial profiles of the temperatures for ions (red curves) and electrons (blue curves), and the temperature ratio T_e/T_i (black curves), and (b) the radial gradient profiles for ion (red) and electron (blue). In both plots, the solid curves represent the results at $t = 4.74$ s in #128670 (helium-dominated case) and the dotted curves represent that at $t = 4.74$ s in #128717 (hydrogen-dominated case).

Here, e_s, T_s, m_s, and $\Omega_s = e_s B/(m_s c)$ represent the electric charge, the equilibrium temperature, the particle mass, and the gyrofrequency of the particle species s, respectively. In the velocity space coordinates, the magnetic moment $\mu = v_\perp^2/2B$ and the parallel velocity $v_\parallel$ are employed. The gyro-averaged potential fluctuation is denoted by $\delta\psi_{k_\perp} = J_{0s}[\delta\phi_{k_\perp} - (v_\parallel/c)\delta A_{\parallel k_\perp}]$ with the zeroth order Bessel function $J_{0s} = J_0(k_\perp v_\perp/\Omega_s)$. And $\omega_{\mathrm{D}s} = \boldsymbol{k}_\perp \cdot \boldsymbol{v}_{s\mathrm{D}}$ and $\omega_{*Ts} = \boldsymbol{k}_\perp \cdot \boldsymbol{v}_{s*}$ are the magnetic and diamagnetic drift frequencies with $\boldsymbol{v}_{s\mathrm{D}} = (c/e_s B)\boldsymbol{b} \times (\mu\nabla B + m_s v_\parallel^2 \boldsymbol{b} \cdot \nabla \boldsymbol{b})$ and $\boldsymbol{v}_{s*} = (cT_s/e_s B)\boldsymbol{b} \times [\nabla \ln n_s + (m_s v^2/2T_s - 3/2)\nabla \ln T_s]$, respectively. In Eq.(1), the symbol $\sum_\Delta$ means double summations respect to $\boldsymbol{k}'_\perp$ and $\boldsymbol{k}''_\perp$, satisfying $\boldsymbol{k}_\perp = \boldsymbol{k}'_\perp + \boldsymbol{k}''_\perp$. Collisional effects are introduced in terms of a linearized model collision operator C_s, where a simplified Lenard-Bernstein model is applied in order to perform the numerical scans for wide-parameter regimes. The Eq. (1) is solved in the local flux-tube coordinates, $\{x, y, z\} = \{a(\rho - \rho_0), a\rho_0 q(\rho_0)^{-1}[q(\rho) - \zeta], \theta\}$ with the flux-coordinates $\{\rho, \theta, \zeta\}$. Here, a is the minor radius, and $q(\rho_0)$ is the safety factor at the focused magnetic flux surface label of ρ_0. The potential fluctuations are calculated by the Poisson and Ampère equations,

$$\left(k_\perp^2 + \lambda_{\mathrm{D}}^{-2}\right)\delta\phi_{k_\perp} = 4\pi \sum_s e_s \int d\boldsymbol{v} J_{0s} h_{sk_\perp}, \tag{2}$$

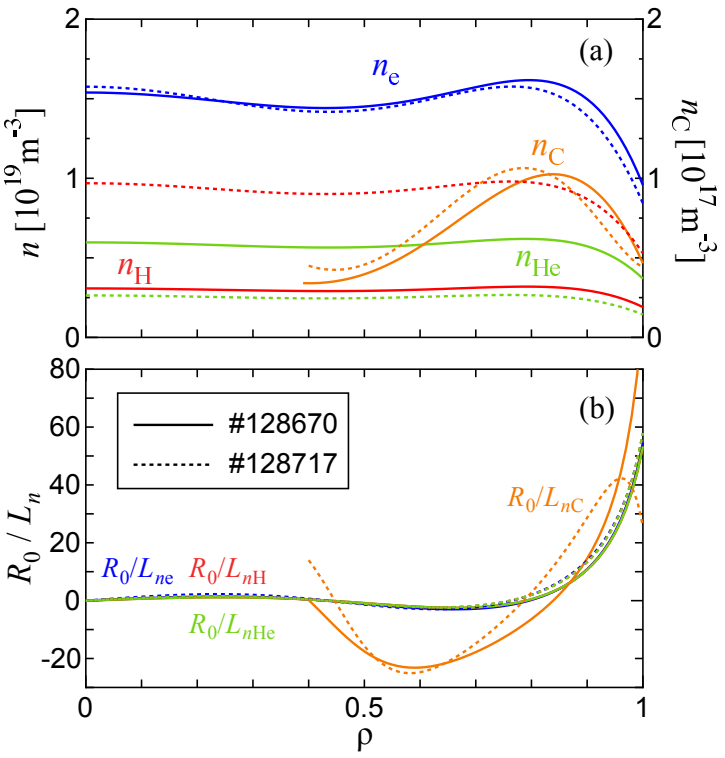

Figure 2. (a) Radial profiles for the densities and (b) the radial gradient profiles of electrons (blue curves), hydrogens (red curves), heliums (green curves), and carbons (orange curves) observed in the LHD experiment of #128670 (solid curves) and #128717 (dashed curves).

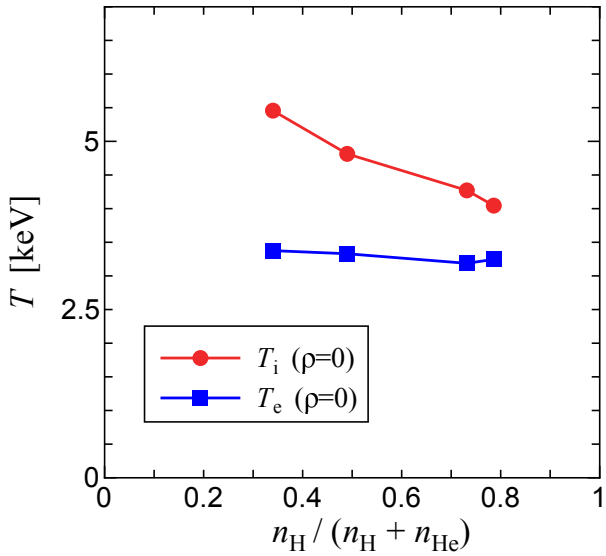

Figure 3. The temperatures at the magnetic axis ($\rho = 0$) for the ions (red circles) and electrons (blue squares) as functions of the hydrogen ion ratio, $n_{\rm H}/(n_{\rm H} + n_{\rm He})$.

$$k_\perp^2 \delta A_{\parallel k_\perp} = \frac{4\pi}{c} \sum_s e_s \int d\boldsymbol{v} v_\parallel J_{0s} h_{sk_\perp}, \tag{3}$$

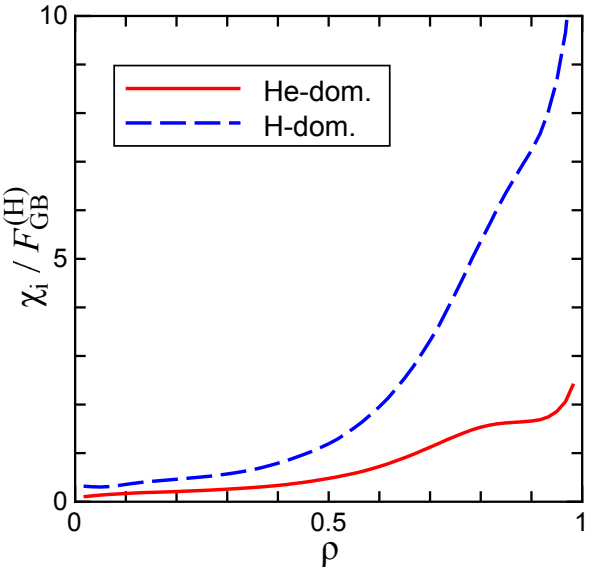

Figure 4. Radial profiles for ion thermal diffusivities estimated by power balance analysis which are normalized by the hydrogen gyro-Bohm factor, $F_{\rm GB}^{\rm (H)} \equiv \alpha(\rho_{\rm t}/R_0)cT_{\rm i}/Z_{\rm H}eB$.

where $\lambda_{\rm D} = (\sum_s 4\pi n_s e_s^2/T_s)^{-1/2}$ is the Debye length for the case of multi-species plasmas. The charge neutrality in the background density n_s is described as $\sum_{s\neq {\rm e}} f_{Cs} = 1$ with the charge-density fraction for ions $f_{Cs} \equiv Z_s n_s/n_{\rm e}$ with the the electric charge Z_s for the species s.

4. Gyrokinetic studies on microinstabilities

In this section, we investigate the ion scale microinstabilities, especially, the ion temperature gradient (ITG) mode in the hydrogen- or the helium-dominated plasmas in the LHD. As discussed in Sec.2, we focused on the LHD experiments of #128670 at $t = 4.74$s as an example of helium-dominated plasmas, and #128717 at $t = 4.74$s as an example of hydrogen-dominated plasmas. We perform the gyrokinetic linear simulations for the multi-species plasmas which includes hydrogen, helium, carbon, and real-mass kinetic electron. In both cases, the temperature and density profiles shown in Fig. 1 are employed. The typical parameters employed in the simulations are shown in Table 1.

Figure 5 shows the results for the normalized growth rates $\gamma R_0/v_{\rm tH}$ and the normalized real frequencies $\omega_{\rm r} R_0/v_{\rm tH}$ of the linear instabilities as functions of the normalized poloidal wavenumber $k_y\rho_{\rm t}$, where $v_{\rm tH}$ is the thermal velocity of hydrogen for each shot. While the real frequencies indicate that the instabilities rotate in the ion diamagnetic direction for both cases, the growth rates are larger in the case of the hydrogen-dominated plasma than in the helium-dominated case. In Fig. 6, the eigenfunctions are evaluated for both cases, and the results indicate the typical structures of the ITG mode which has strong ballooning structures, where there do not exist the clear differences from each other.

Table 1. Typical parameters at $\rho = 0.48$ for both hydrogen- and helium-dominated cases employed in the simulations. Here, $Z_{\rm eff} \equiv \sum_{s\neq {\rm e}} f_{Cs} Z_s$ represents the effective ion charge.

	q_0	$\hat{s}$	r/R_0	$T_{\rm e}/T_{\rm i}$	$\nu^*_{\rm H\text{-}He}$	$Z_{\rm eff}$
#128670	2.0	-0.580	0.0807	0.829	0.0347	1.86
#128717	2.0	-0.583	0.0812	1.104	0.0288	1.44
	R_0/L_{Te}	R_0/L_{Ti}	R_0/L_{ne}	$R_0/L_{n\rm H}$	$R_0/L_{n\rm He}$	$R_0/L_{n\rm C}$
#128670	4.026	10.113	-0.782	-0.5628	-0.5630	-14.625
#128717	4.224	11.200	-0.943	-0.7661	-0.7660	-10.378

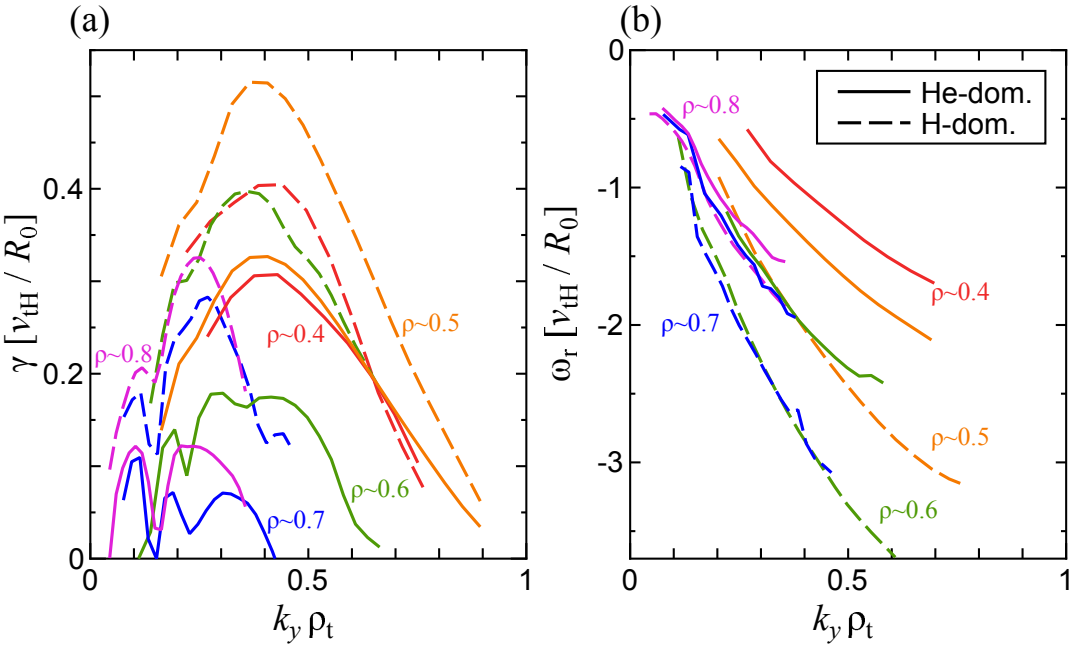

Figure 5. (a) Growth rates and (b) real frequencies of the linear instabilities as functions of the normalized poloidal wavenumber $k_y\rho_{\rm t}$ with $k_x = 0$ at several radial positions, $\rho \sim 0.4$ (red), 0.5 (orange), 0.6 (green), 0.7 (blue), and 0.8 (magenta) in the LHD experiments. In both plots. the solid curves represent the observations at $t = 4.74$ s in the helium-dominated plasma and the dashed curves represent the observations at $t = 4.74$ s in the hydrogen-dominated plasma.

In order to clarify the dependencies on the ion-mass number and the electric charge for the plasma which consists of multi-ion-species, the turbulent transport driven by the ITG mode can be evaluated according to the mixing length estimate[21],

$$\chi \sim \frac{\gamma}{k_\perp^2} = \frac{\bar{\gamma}}{\bar{k}_\perp^2}\left(\frac{\rho_{\rm ts}^2 v_{\rm ts}}{R_0}\right) = \frac{\bar{\gamma}}{\bar{k}_\perp^2}\frac{\sqrt{A_s}}{Z_s^2}\left(\frac{\rho_{\rm t}^2 v_{\rm tH}}{R_0}\right), \tag{4}$$

where A_s denotes the mass number of the species s. Here, the normalized growth rates and the wavenumber are defined by $\bar{\gamma} \equiv \gamma(v_{\rm ts}/R_0)$ and $\bar{k}_\perp \equiv k_\perp \rho_{\rm ts}$, respectively. Therefore, the normalized $\bar{\gamma}/\bar{k}_\perp^2$ does not depend on the factor of $\sqrt{A}/Z^2$, while $\gamma/k_\perp^2$

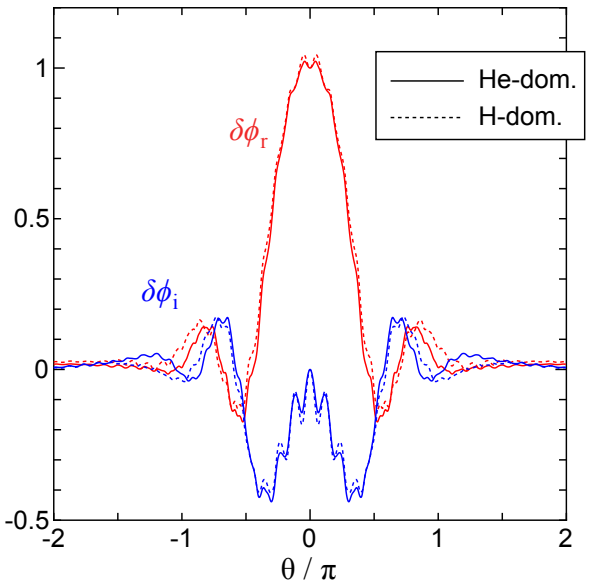

Figure 6. The eigenfunctions of the electrostatic potential fluctuation, $\delta\phi = \delta\phi_r + i\delta\phi_i$ at $(k_x\rho_t, k_y\rho_t) = (0, 0.407)$ for the cases of #128670 (solid curves) and #128717 (dotted curves). The red curves and the blue curves represent the real parts and the imaginary parts of the functions, respectively.

has the dependencies on the factor. Of course, the normalized $\bar{\gamma}/\bar{k}_\perp^2$ can depend on the other factors such as the temperature ratio T_e/T_i. Using the charge densities f_{Cs} from the experimental observations, we can evaluate the effective factors of $\sqrt{A}/Z^2$ in the mixed-species plasmas defined by $(\sqrt{A}/Z^2)_{\rm eff} \equiv \sum_{s\neq e} f_{Cs}\sqrt{A_s}/Z_s^2$. The results at $\rho \sim 0.48$ are $(\sqrt{A}/Z^2)_{\rm eff}^{\rm (He\text{-}dom.)} = 0.59$ and $(\sqrt{A}/Z^2)_{\rm eff}^{\rm (H\text{-}dom.)} = 0.81$.

Figure 7(a) shows the wavenumber spectra of the the mixing length estimate $\gamma_k/k_y^2(R_0/\rho_t^2 v_{tH})$ at $\rho = 0.48$, where the ITG modes are most unstable in both cases. The mixing length diffusivity in the helium-dominated case is smaller than the hydrogen-dominated case by the ratio $\chi^{\rm (He\text{-}dom.)}/\chi^{\rm (H\text{-}dom.)} \sim 0.6$. Since the mixing length diffusivities are normalized by $\rho_t^2 v_{tH}/R_0$ which has ion temperature dependence $\sim T_i^{3/2}$, we can evaluate the diffusivities at same ion temperature by multiplying the factor of the ion temperature ratio, $(T_i^{\rm (H\text{-}dom.)}/T_i^{\rm (He\text{-}dom.)})^{3/2}$. As shown in the figure, we confirm that such normalized diffusivities in both cases close to each other. Furthermore, based on the discussions for a reduced transport model[9], we evaluate $\sum_k \gamma_k/k_y^2(R_0/\rho_t^2 v_{tH})$ for both cases to estimate the radial profiles of the diffusivities. Since we obtain the experimental results for the total ion heat diffusivities shown in Fig. 4, we plot in Fig.7(b) showing the radial profiles of $\sum_k \gamma_k/k_y^2(R_0/\rho_t^2 v_{tH})$ and the results of the power balance analyses. It can be confirmed that the trends of the profiles are similar to the results of the power balance analyses.

To evaluate the dependencies of the mixing length diffusivity on the ion temperature gradient scale lengths, we performed the linear simulations with changing R_0/L_{Ti} as shown in Fig. 8. In the helium-dominated case, the mixing length diffusivities are smaller than the hydrogen-dominated case for wide range of the temperature gradients.

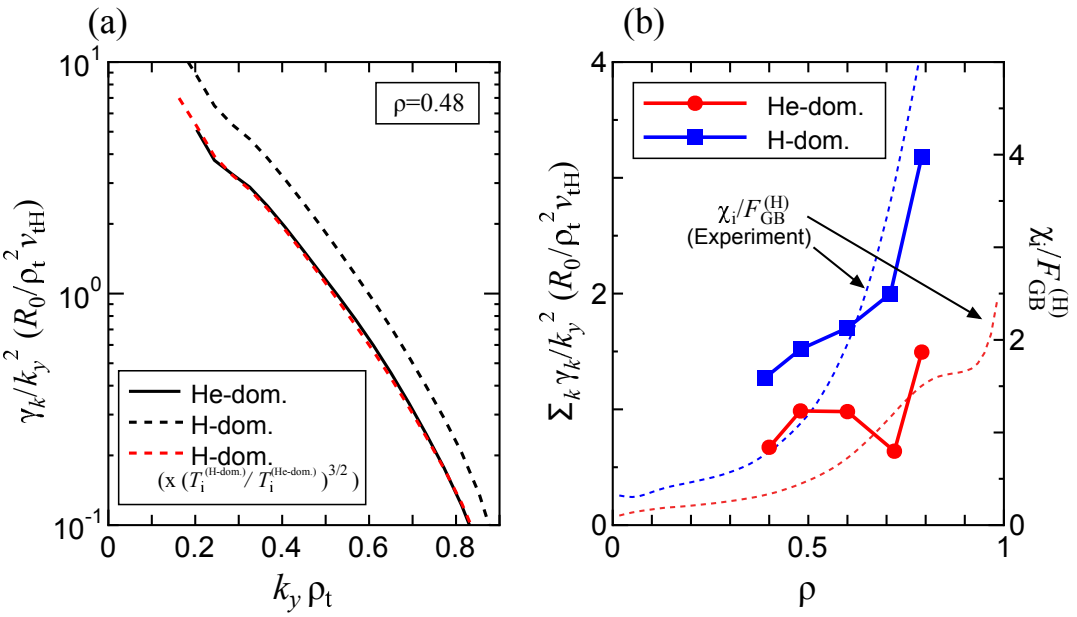

Figure 7. (a) The poloidal wavenumber spectra of γ_k/k_y^2 at $\rho = r/a = 0.48$ in the helium-dominated case (solid curve) and the hydrogen-dominated case (dotted curve), and (b) radial profiles of $\sum_k \gamma_k/k_y^2$ for the helium-dominated case (red circles) and the hydrogen-dominated case (blue squares). In (a), the red dashed curve represents the spectrum in the hydrogen-dominated case multiplied by the factor of the ion temperature ratio, $(T_i^{(\text{H-dom.})}/T_i^{(\text{He-dom.})})^{3/2}$. In (b), the dotted curves show the ion heat diffusivities for each case in the hydrogen gyro-Bohm unit $\chi_i/F_{GB}^{(H)}$ as same as Fig. 4.

On the other hand, the temperature ratio between the electron and the ions T_e/T_i also affect the diffusivities. If we apply the ratio T_e/T_i of the hydrogen-dominated case to the helium-dominated plasma, the diffusivities are increased from the original one as shown in the Fig. 8. While the diffusivity increased by the changing T_e/T_i is close to the diffusivity in the hydrogen dominated case for near-marginal temperature gradient, the diffusivity with changing T_e/T_i tends to leave from that of the hydrogen dominated case for higher ion temperature gradient region. Therefore, since the other parameters, e.g., configuration parameters, density gradients, etc., are nearly the same each other in the plots, the effect of the ratio T_e/T_i on the mixing length diffusivities is dominant for near-marginal temperature gradient, the differences of the mass number and the electric charge of the ion species affect the diffusivities for higher R_0/L_{Ti}. The rates of the diffusivities between each case at the fixed temperature gradient of $R_0/L_{Ti} = 10.0$ are $\mathcal{R}' \equiv (\gamma/k_y^2)'_{\text{He-dom.}}/(\gamma/k_y^2)_{\text{H-dom.}} \sim 0.89$ and $\mathcal{R} \equiv (\gamma/k_y^2)_{\text{He-dom.}}/(\gamma/k_y^2)_{\text{H-dom.}} \sim 0.76$. Here, $(\gamma/k_y^2)'_{\text{He-dom.}}$ is obtained in the helium dominant case with T_e/T_i of the hydrogen-dominant one. Indeed, the ratios $\mathcal{R}$ and $\mathcal{R}'$ are larger than the simple analyses expectation based on the gyro-Bohm scaling, Eq.(4), namely, $\mathcal{R}_{\text{GB}} = (\sqrt{A}/Z^2)_{\text{eff}}^{(\text{He-dom.})}/(\sqrt{A}/Z^2)_{\text{eff}}^{(\text{H-dom.})} \sim 0.73$. On the other hand, for higher $R_0/L_{Ti} = 15.0$, we find the more enhanced ratio, $\mathcal{R}' \sim 0.86$ and $\mathcal{R} \sim 0.73$.

As a reference, in addition to the mixing length estimates, we evaluate a simple

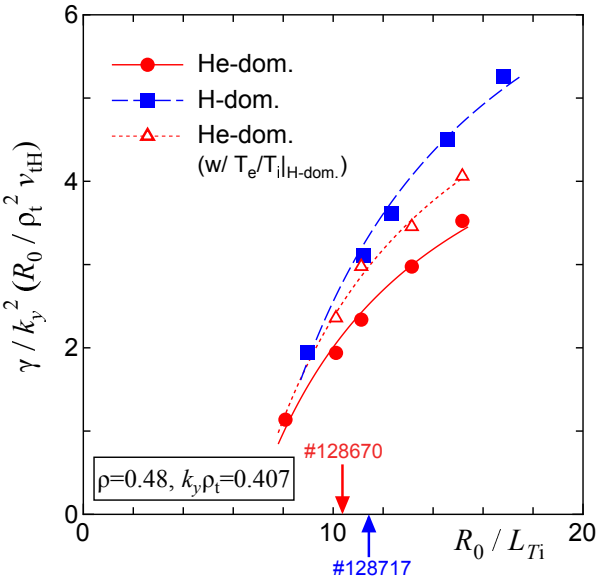

Figure 8. Ion temperature gradient dependences of the mixing length diffusivities in the helium-dominated case (red solid curve with circles) and the hydrogen-dominated case (blue dotted curve with squares) at $\rho = 0.48$ and $k_y\rho_t = 0.407$. The red dotted curve with the triangles shows the results in the helium-dominated case with same T_e/T_i in the hydrogen-dominated case.

quasi-linear total ion heat fluxes [22] which is written by $Q_i^{(QL)} \equiv \sum_{s\neq e} Q_s^{(QL)} = \sum_{s\neq e}\sum_k (Q_s^{(lin.)}/\langle|\delta\phi_k^{(lin.)}|^2\rangle)(\gamma_k R_0/k_y^2\rho_t^2 v_{tH})$. Here, $Q_s^{(lin.)}$ is the heat flux for the ion species s calculated by the linear gyrokinetic simulations. In Fig. 9, the normalized quasi-linear total ion heat fluxes in both cases are plotted with changing the ion temperature gradient lengths. The quasi-linear fluxes can change more than 50% for the helium-dominated case, and 90% for the hydrogen-dominated case within the ranges of R_0/L_{Ti} of $\pm 20\%$. Of course, in order to evaluate quantitative transport fluxes and precise comparisons between the experiments and the simulations, the nonlinear gyrokinetic simulations are strongly demanded.

5. Summary

In this paper, using the gyrokinetic plasma turbulence code which can treat the multi-species plasmas including real-mass kinetic electrons, we performed the linear simulations for the microinstabilities in the multi-species plasma which consists of hydrogen, helium, carbon impurity ions and electron in the LHD. In the helium-dominated plasma with higher achieved ion temperature including the multi-species ions, the growth rates of the microinstabilities driven by the ITG mode are smaller than the hydrogen-dominated one. In the analyses of the mixing length diffusivity and its sensitivities to the ion temperature gradients, it is also confirmed that the ion heat diffusivities normalized by the hydrogen gyro-Bohm unit can be reduced in the helium-dominated plasma from the hydrogen-dominated one. The weakened

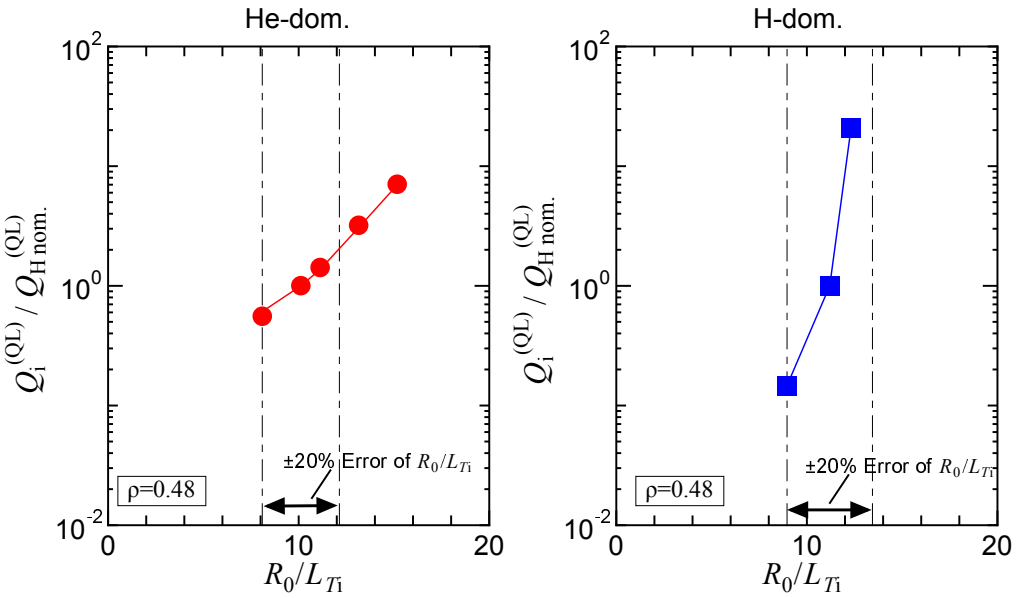

Figure 9. Quasi-linear total ion heat fluxes with changing ion temperature scale lengths in the helium-dominated case (left) and the hydrogen-dominated case (right). $Q_{\rm i}^{\rm (QL)}$ is normalized by $Q_{\rm Hnom}^{\rm (QL)}$ which is the heat fluxes at the nominal parameters of $R_0/L_{T\rm i}$ correspond to each case.

diffusivities in the helium dominated case are caused by not only the effect of the differences for the mass number and the electric charge of the mixed-ions, but also the difference of the temperature ratio $T_{\rm e}/T_{\rm i}$. The results is qualitatively consistent with the LHD experimental observations that the heat transport diffusivities in the hydrogen gyro-Bohm unit are reduced in the helium-dominated plasma comparing the hydrogen-dominated case. The higher $T_{\rm i}$ at the edge region in the helium-dominated case may cause the core high-$T_{\rm i}$ with same level of the $T_{\rm i}$-gradient scale lengths with the hydrogen-dominated case, owing to reduction of the ITG turbulent transport due to low $T_{\rm e}/T_{\rm i}$-ratio. The simulations employed in this paper are restricted to the linear instability analyses, it should be extended to more precise transport analyses based on the nonlinear simulations under variation of the parameters, e.g., collisionality, field configurations, and so on. On the other hand, the zonal flows also play a significant role on the transport reduction in helical plasmas[23, 24]. In order to treat favorable effects of heavier hydrogen isotopes on plasma confinement improvement, we also should perform gyrokinetic simulation analyses with zonal flows and/or background $\boldsymbol{E} \times \boldsymbol{B}$ rotations taken into account as pointed out in Refs. of [25, 26]. The nonlinear simulations and more extended analyses for quantitative validation of the simulation will be reported elsewhere.

Acknowledgments

This work is supported in part by the Japanese Ministry of Education, Culture, Sports, Science and Technology (MEXT), Grant (Nos. 26820398, 26820401 and 16K06941),

by National Institute for Fusion Science (NIFS) Collaborative Research Program (KNST095, KNTT031, KNTT035), by use of Helios system at International Fusion Energy Research Center (Project code: GKMLDST, GKVPP, VLDGK, VLDGK_ST, and GTNAXIS), and by the FLAGSHIP2020, MEXT within the priority study 6.

[1] X. Garbet, Y. Idomura, L. Villard, and T.H. Watanabe, Nucl. Fusion **50**, 043002 (2010).
[2] T.L. Rhodes, C. Holland, S.P. Smith, A.E. White, K.H. Burrell, J. Candy, J.C. DeBoo, E.J. Doyle, J.C. Hillesheim, J.E. Kinsey, G.R. McKee, D. Mikkelsen, W.A. Peebles, C.C. Petty, R. Prater, S. Parker, Y. Chen, L. Schmitz, G.M. Staebler, R.E. Waltz, G. Wang, Z. Yan and L. Zeng, Nucl. Fusion **51**, 063022 (2011).
[3] T. Görler, A. E. White, D. Told, F. Jenko, C. Holland and T. L. Rhodes, Phys. Plasmas **21**, 122307 (2014).
[4] M. Nunami, T.-H. Watanabe, H. Sugama and K. Tanaka, Plasma Fusion Res. **6**, 1403001 (2011).
[5] M. Nunami, T.-H. Watanabe, H. Sugama, and K. Tanaka, Phys. Plasma **19**, 042504 (2012).
[6] A. Ishizawa, T.-H. Watanabe, H. Sugama, M. Nunami, K. Tanaka, S. Maeyama and N. Nakajima, Nucl. Fusion **55**, 043024 (2015).
[7] C. Holland, Phys. Plasmas **23**, 060901 (2016).
[8] M. Nakata, M. Honda, M. Yoshida, H. Urano, M. Nunami, S. Maeyama, T.-H. Watanabe and H. Sugama, Nucl. Fusion **56**, 086010 (2016).
[9] M. Nunami, T.-H. Watanabe, and H. Sugama, Phys. Plasma **20**, 092307 (2013).
[10] A. Komori, H. Yamada, S. Imagawa, O. Kaneko, K. Kawahata, K. Mutoh, N. Ohyabu, Y. Takeiri, K. Ida, T. Mito, Y. Nagayama, S. Sakakibara, R. Sakamoto, T. Shimozuma, K. Y. Watanabe, O. Motojima for LHD Experiment Group, Fusion Sci. Technol. **58**, 1 (2010).
[11] M. Osakabe, *et al.*, the 25th International Toki Conference, invited talk (I-1), 3rd Nov. 2015, Toki, Japan.
[12] M. Nakata, M. Nunami, H. Sugama, and T.-H. Watanabe, Plasma Phys. Control. Fusion **58**, 074008 (2016).
[13] K. Nagaoka, H. Takahashi, K. Tanaka, M. Osakabe, S. Murakami, S. Maeta, M. Yokoyama, K. Fujii, H. Nakano, H. Yamada, Y. Takeiri, K. Ida, M. Yoshinuma, and the LHD Experiment Group, Plasma Fusion Res. **11**, 2402106 (2016).
[14] K. Tanaka, K. Nagaoka, S. Murakami, *et al.*, 26th IAEA Fusion Energy Conference, P8-437 (2016), submitted to Nuclear Fusion.
[15] M.Yokoyama, R. Seki, C. Suzuki, *et al.*, Plasma Fusion Res. **9**, 3402017 (2014).
[16] T.-H. Watanabe and H. Sugama, Nucl. Fusion **46**, 24 (2006).
[17] M. Nunami, T.-H. Watanabe, and H. Sugama, Plasma Fusion Res. **5**, 016 (2010).
[18] A. Ishizawa, T.-H. Watanabe, H. Sugama, M. Nunami, K. Tanaka, S. Maeyama and N. Nakajima, Nucl. Fusion **55**, 043024 (2015).
[19] M. Nunami, M. Nakata, T.-H. Watanabe, and H. Sugama, Plasma Fusion Res. **10**, 1403058 (2015).
[20] M. Nakata, M. Nunami, T.-H. Watanabe, and H. Sugama, Comput. Phys. Comm. **197**, 61 (2015).
[21] J. Wesson, *Tokamaks Second Edition* (Oxford University Press, 1997), pp.198.
[22] D.R. Mikkelsen, K. Tanaka, M. Nunami, *et al.*, Phys. Plasma **21**, 082302 (2014).
[23] T.-H. Watanabe, H. Sugama, and S. Ferrando-Margalet, Phys. Rev. Lett. **100**, 195002 (2008).
[24] P. Xanthopoulos, A. Mishchenko, P. Helander, H. Sugama, and T.-H. Watanabe, Phys. Rev. Lett. **107**, 245002 (2011).
[25] H. Sugama, and T.-H. Watanabe, Phys. Plasma **16**, 056101 (2009).
[26] T.-H. Watanabe, H. Sugama, and M. Nunami, Nucl. Fusion **51**, 123003 (2011).